# Surface Topology as Non-Destructive Proxy for Tensile Strength of Plastic Parts from Filament-based Material Extrusion

Bevan Harbinson,<sup>1</sup> Sierra F. Yost,<sup>2</sup> Bryan D. Vogt<sup>2,\*</sup>(ORCID: 0000-0003-1916-7145)

## Acknowledgements

This work was partially supported by the National Science Foundation under grant no. CMMI-2011289. The authors acknowledge use of the Penn State Materials Characterization Lab for tensile measurements.

<sup>&</sup>lt;sup>1</sup>Department of Materials Science and Engineering, The Pennsylvania State University, University Park, PA 16802

<sup>&</sup>lt;sup>2</sup>Department of Chemical Engineering, The Pennsylvania State University, University Park, PA 16802

<sup>\*</sup>To whom correspondence should be addressed: <a href="mailto:bdv5051@psu.edu">bdv5051@psu.edu</a> (B.D.V.)

Surface Topology as Non-Destructive Proxy for Tensile Strength of Plastic Parts from Filamentbased Material Extrusion

#### **ABSTRACT**

Non-destructive characterization of 3D printed parts is critical for quality control and adoption of additive manufacturing (AM). The low-cost driver for AM of thermoplastics, typically through material extrusion AM (MEAM), challenges the integration of real-time, operando characterization and control schemes that have been developed for metals. Here, we demonstrate that the surface topology determined from optical profilometry provides information about the mechanical response of the printed part using commercial ABS filaments through calibration based correlations. The influence of layer thickness was examined on the tensile properties of MEAM ABS. Surface topology was converted into amplitude spectra using fast Fourier transforms. The scatter in the tensile strength of the replicate samples was well represented by the differences in the amplitude of the two fundamental waves that describe the periodicity of the printed roads. These results suggest that information about previously printed layers is transferred to subsequent layers that can be resolved from optical profilometry and offers the potential of a rapid, nondestructive post-print characterization for improved quality control.

**KEYWORDS**: optical profilometry; Fourier image analysis; fused filament fabrication (FFF); fused deposition modeling (FDM)

## 1. INTRODUCTION

3D printing enables the near net shape manufacture of customized products [1-3] and potential to improve sustainability metrics in manufacturing [4, 5]; extrusion of thermoplastics represents one of the least expensive modes of additive manufacture [6, 7], especially with respect to initial capital investment. However, the surface finish [8] and mechanical properties from material extrusion additive manufacturing (MEAM) of thermoplastics tend to be inferior to traditional plastic manufacture [9, 10]. Significant efforts have gone into the optimization of print conditions

[11, 12] and formulating plastics [13-15] to improve mechanical performance. Parameterization of the processing space has demonstrated the importance of extrusion temperature [16], print bed temperature [17], environmental temperature [18], print speed [19], and orientation [20, 21] on properties. In addition to challenges associated with processing sensitivity, there are additional issues associated with relatively large variability in properties even at essentially equivalent print conditions for MEAM.

The quality of the filaments [22] can significantly impact the variance in properties due to changes in the volumetric flow associated with local deviations in the filament diameter. Although optical characterization of the filament [22, 23] as it is fed into the hotend could provide a route to adjust the extrusion rate on the fly, this would significantly increase costs and require custom integration with the printer. Inline measurement of pressure during printing [24, 25] can provide insights into variation in the filament diameter as well; coupling these pressure measurements with inline temperature and viscosity measurements can predict the interlayer strength [24], which defines the mechanical performance of the parts. However, these measurements require custom modification of printers, which may void manufacturer warranties and any feedback control beyond a simple quality control for rejection of a part would necessitate understanding of how to compensate for variations. Quantitative models that can describe MEAM are being developed [26-28], but require significant complexity to address the elasticity of the polymer melt and rate dependent viscoelastic properties [29] that will describe the print through complex shapes where corners require variation in printing rate [30]. Inclusion of chain-level dynamics provides a route to include residual orientation of chains [31] that impact the interfacial weld strength. The models typically include significant simplifications due to the complexity associated with non-isothermal, non-steady state polymer flow in modeling the whole printing process, but these can be helpful in providing heuristics that assess printability [32] and other characteristics [33].

These characteristics provide challenges for model-based quality control to provide rejection of inferior parts for MEAM, especially for critical applications where internal defects could threaten the required service performance [3]; both x-ray computed tomography (µCT) [34] and

ultrasound [35] provide a route to identify internal defects, but  $\mu$ CT is expensive and interpretation of ultrasound can be challenging for complex parts. These techniques along with optical imaging can be applied as inline metrology for determination of subsurface and internal defects [36]. Defect detection has been a critical area of research for metal AM [37, 38] for quality diagnostics [39] with inline detection, analysis and methods for on-the-fly corrections to the print developed [40]. Defects are known to be detrimental to parts produced by MEAM with a variety of strategies developed to reduce defects through print path, process parameters and post-processing [41]. Inline control strategies for bioprinting have been developed [42] to identify errors and correct during printing, but these strategies can be cost prohibitive for more commodity 3D printing applications.

New routes are desired to cost effectively and non-destructively assess properties of 3D printed parts to reduce overdesign resulting from the large variance in final properties that can be obtained under essentially identical process conditions [34]. It is well known that critical defects in one layer can translate into print failures in subsequent layers, but how much information about minor non-idealities in the print is transferred to subsequent layers has not been extensively investigated. Here, we examine the surface morphology of printed samples with optical profilometry, which offers the potential for rapid and reasonably inexpensive post-print characterization. The images were analyzed to understand if there is hidden information within the surface structure that arises from the printing process that provides insights into the mechanical properties. Through analysis of the surface topology in Fourier space, a correlation involving the road width and period of two roads is found to describe the tensile strength of printed parts including much of the variance in properties at the same print conditions. Here we use the term "road" to describe the physical bead of plastic material deposited by the hotend along the print path. These results suggest that additional information may be hidden within the surface topology of 3D printed parts that could be used to provide facile quality control metrics where profilometry could be used directly after AM to screen for low performing parts after appropriate calibration of the surface topology to properties of interest.

## 2. EXPERIMENTAL SECTION

Hatchbox True Blue ABS filament (1.75 mm diameter, HATCHBOX 3D, Pomona, CA, USA) was used for the printing. The filament was dried overnight at 80 °C in a vacuum oven prior to use. The drying is to remove the limited amount of sorbed water within the ABS filament during printing that can lead to reduced mechanical properties [43]. A Roboze One+400 Xtreme 3D printer (Roboze, Bari, Apulia, Italy) with a 0.4 mm diameter nozzle was used to print the ABS at an extruder temperature of 225 °C and a print bed temperature of 90 °C. The printed specimens were ASTM D638-22 Type V tensile bars with a thickness of 2 mm, XY (flat) build orientation, and 100% infill [44]. The print speed was 60 mm/s. A summary of process parameters is listed in the Supplementary Materials. Three different layer thicknesses (0.2, 0.25, and 0.3 mm) were examined. The G-code and print path were generated using Simply3D software. As the weld line between the roads is typically the weak spot mechanically, the tensile specimens were printed at 90° raster angle. Figure 1 illustrates the appearance of a representative printed tensile bar. There was no readily apparent difference in the specimens with different layer thicknesses from these images. Tensile specimens were printed sequentially to produce 5 specimens per condition. The gauge region of the printed specimens was found to be  $3.08 \pm 0.02$  mm wide and  $1.99 \pm 0.09$  mm thick, which is within the tolerances prescribed by ASTM D638-22.



**Figure 1.** Image of 3D printed tensile bar using a layer thickness of 0.3 mm and 90° raster angle. The coordinate axes describe the raster angle relative to the direction of the deformation during tensile testing. The shaded box with dashed lines illustrates the area of the top surface of the printed specimens that is characterized by optical profilometry.

The top layer of the gauge sections of each specimen were imaged prior to any deformation using a Zeta-20 Optical Profiler (Zeta Instruments, San Jose, CA, USA). This profilometer is distinct from more common stylus profilometers that provide line scans with height vs. distance through

contact of a probe stylus with the surface. Optical profilometry used here is non-contact and generates data in three dimensions associated with the illuminated area of the surface being measured and the local height in the area. The use of an opaque plastic filament in this case facilitates the measurement to avoid any scattering and reflections of light from within the bulk of the specimen. In this work, a 50x magnification objective lens with a numerical aperture of 0.8 and working distance of 1.0 mm was used for all profilometry measurements. The spatial resolution was 0.364 µm. To increase the field of view with this optical profilometer, 80 overlapping images (20 x 4 grid) were captured and manually aligned to generate a topological map over 8390 μm x 1080 μm area centered within the gauge section with the x-axis perpendicular to the print direction. The topological images were captured using the ZDot™ interference technique that modulates the focal plan using a piezoelectric stepper motor to produce a height map with a 0.364 µm resolution in x-y plane and 25 nm height resolution. This topology measurement from profilometry is related to the surface examined and does not probe the full thickness of the specimens. The location of the examined area (8390 μm x 1080 μm) is shown schematically by the rectangular box in Figure 1. The profilometer profiles were anisotropic due to the directionality of the print.

In order to better visualize the profilometry data and the periodicity associated with the print path, the 3D topological map from the profilometer for each specimen was sliced into a series of line profiles perpendicular to the printed road every 20 µm across the width of the gauge section. These line profiles were further analyzed with Fourier transforms as this provides a simple method to provide image analysis of the 3D printed parts [45] and these transforms have been previously successfully applied to vision-based process monitoring [46]. To improve the accuracy of the fast Fourier transform (FFT), the obtained line profiles were cropped to 8000 µm to provide unit fractions for the FFT [47]. A discrete Fourier transform (DFT) of each line profile was then computed using the Fastest Fourier Transform in the West (FFTW) library in MATLAB [48]. The discrete Fourier transform was used in this case due to the anisotropy in both the topology itself and the area imaged. The narrow width of the gauge region of the tensile bar limits the size of the topological image possible. Each DFT was converted into a single-sided amplitude spectrum

(SSAS) describing the amplitude of each wave present in the surface with respect to frequency. The combination of the SSASs forms a 3D representation of the surface topology associated with the inter-road structure in Fourier space.

Uniaxial tensile testing was conducted following ASTM D638-22 standards. The specimens were extended at 5 mm/min under ambient conditions using an MTS Criterion Model 43 load frame (MTS Systems, Eden Prairie, MN, USA) equipped with a 1000 N load cell, self-tightening scissor action grips, and an MTS Advantage Video Extensometer 204. The specimens were not dried after printing. The mechanical tests for all of the specimens occurred over two consecutive days to minimize any environmental factors as high humidity can alter the stiffness of printed ABS, but does not significantly impact the tensile strength [49]. The gauge section of each specimen was marked with a small dot of liquid white out (Bic) for tracking the strain with the extensometer. Engineering stress-strain curves for each specimen were generated using the load data, each specimen's cross-sectional area, and strain data from the extensometer. The elastic modulus (E), ultimate tensile strength ( $\sigma_{\text{U}}$ ), and elongation at break ( $\epsilon_{\text{D}}$ ) were calculated from these curves.

#### 3. RESULTS AND DISCUSSION

The mechanical performance and surface finish of 3D printed parts can be impacted by the selection of the layer thickness [50]; moreover, as the layer thickness decreases, the print time for the same part increases significantly. The ABS specimens were printed at conditions (T<sub>extrusion</sub> = 225 °C and T<sub>bed</sub> = 90 °C) recommended by the manufacturer. Figure 2 illustrates the tensile stress-strain curves for ABS printed at 90° raster angle for different layer thicknesses. The curves for multiple specimens are shown for each condition to illustrate the reproducibility of the response. The noise in the curves is associated with vibrations in the video extensometer which tracks the deformation only in the gauge region; this noise is not present in strain determined from the crosshead motion as shown in Figure S1. For these tensile bars, Figure S1 illustrates significant difference in the strain between the video extensometer and the crosshead due to deformation in the grip region that is not included with the video extensometer. Thus, we have used the strain from the video extensometer for the calculation of the mechanical properties of

the 3D printed parts. Interestingly, the largest layer thickness examined led to the most ductile response on average. This can be rationalized in terms of the number of interfaces generated during the print; the thicker layer thickness decreases the number of layers required to be printed for the same total dimensions for the tensile bars and the part behaves as a laminated composite [51].

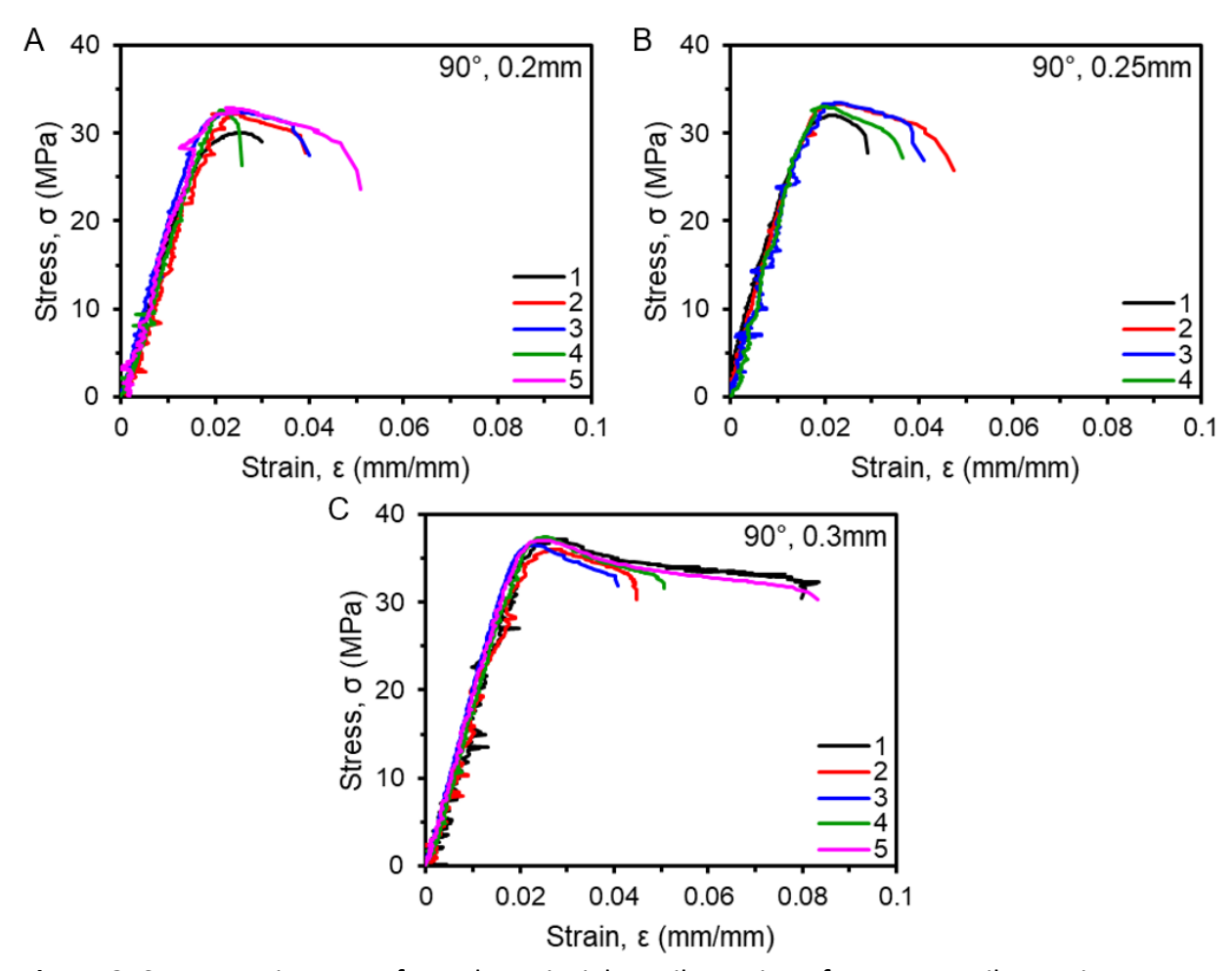


**Figure 2.** Stress-strain curves from the uniaxial tensile testing of Type V tensile specimens following ASTM D638-22 using layer thicknesses of (A) 0.2 mm, (B) 0.25 mm and (C) 0.30 mm. The raster angle was 90°. Multiple specimens were printed under the same conditions and shown in different colors.

Typically, there is large anisotropy in the mechanical properties for MEAM plastics between 0° and 90° raster angle with 90° orientation tending to result in significantly reduced mechanical performance. For this commercial ABS, we find only minor differences in the mechanical response

with the raster angle as well as the layer thickness for these Type V tensile bars as shown in Figure 3. The raw tensile data for the 0° raster angle are shown in Figure S2. This lack of sensitivity is unusual, but significant engineering in the formulation of commercial filaments can involve additives [44] to enhance diffusion and reduce anisotropy in part performance, which may explain the limited effect of raster angle along with the short time between printing adjacent roads with the Type V dogbones. In examination of Figure 2, the part-to-part variation can be more significant than the differences based on raster angle and layer thickness.

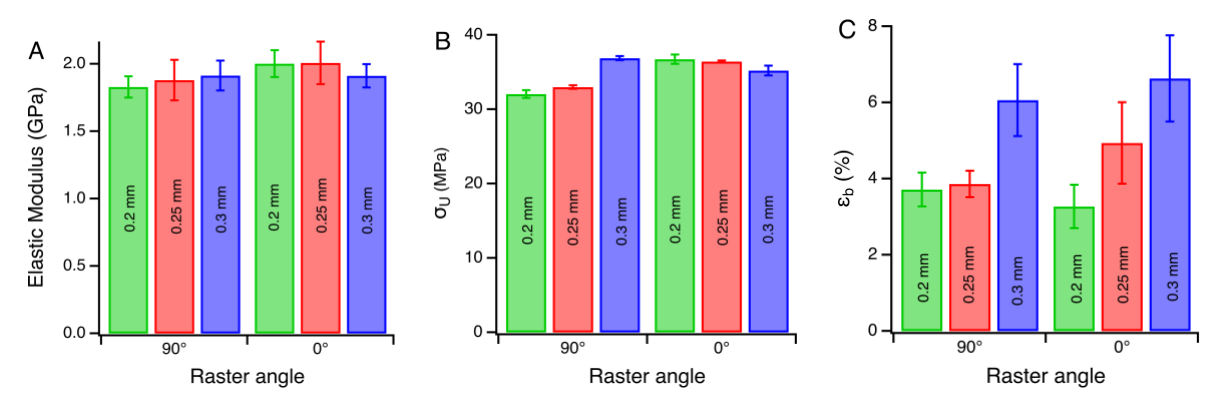


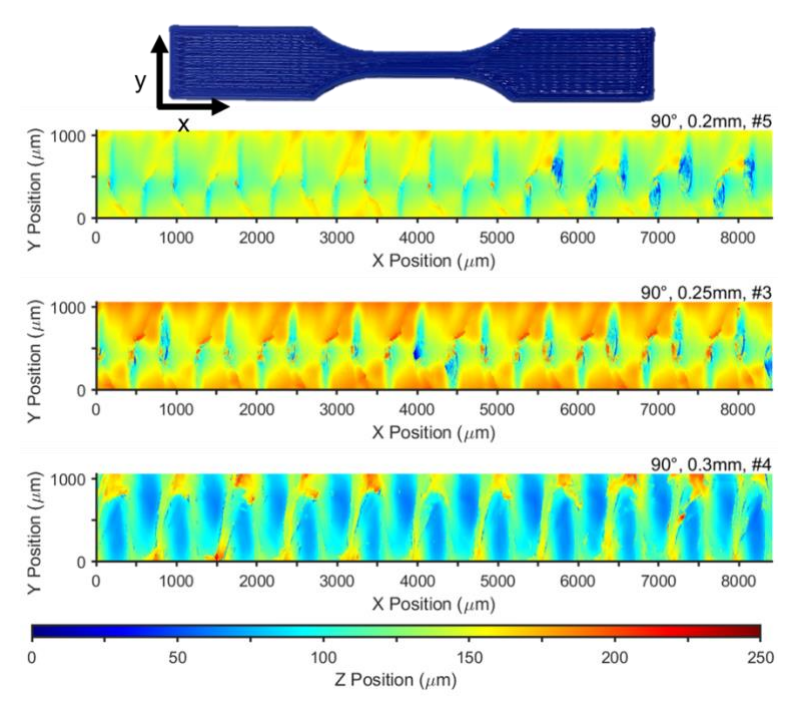
**Figure 3.** Influence of raster angle and layer thickness on (A) elastic modulus, (B) ultimate tensile stress, and (C) strain at break. The error bar represents the standard error in the measurement.

This variation in properties between effectively identical parts with the same processing parameters could be a limiting factor for the engineering design and thus it would be beneficial to be able to identify the poor performing parts non-destructively for quality control directly after printing and before the part enters the supply chain. As many adaptive control algorithms for onthe-fly error correction [36, 52] assume that errors build up, effectively indicating information transfer between layers, the surface morphology of a printed part could include information about underlying layers that could act to provide predictive capabilities for other properties of the part. The limited effect of layer thickness on properties, while there is reasonable large variance in some mechanical properties for these ABS specimens offers a platform to test this concept that the surface topology contains information about underlying layers. However, despite the similarities in properties, the surface topology is distinct for the three different layer thicknesses examined as shown in Figure 4. These images of the surface topology were taken prior to mechanical testing and represent the top surface morphology post-print. The use of the

Type V tensile bar allows for easy imaging across nearly the full width of the gauge section, so the dynamics of the print process involving the edges can be visualized. As we are interested in the relationships to the mechanical properties and the print process parameters are known to be strongly correlated with these properties [7], the top surface of the printed specimens were examined without any post-processing.

The general shape of the surface topology changes with the layer thickness as shown in Figure 4. These surface features are not parallel to each other, but rather exhibit asymmetric curvature associated with the acceleration and deceleration as the hotend starts on a road and then slows as the edge of the specimen is reached. This morphology contrasts with examination of the middle of the grip section of the dogbone specimens, where parallel roads run across the profile as shown in Figure S9. The surface of the 0.2 mm specimen (Figure 4A) is flat and relatively smooth with excellent intra-layer contact on the left side of the image, but the morphology shifts slightly around  $x = 5000 \mu m$ . After this point, periodic ovoid holes remain unfilled in the specimen as shown by the dark blue regions. The 0.25 mm layer thickness specimen has a similar morphology that is flat in most areas with small ovoid holes between each road (dark blue regions in Figure 4B). The increase in layer thickness to 0.3 mm yields a drastic change in surface morphology with no holes open to the underlying layers, only what can be described as flatbottomed valleys. Part of difference in the structure between these two specimens is the noise present in and around holes due to the steep slopes of the surface in those regions [53], which can be considered as artifacts. The overall variation in the surface features is marginally greater for the 0.25 mm layer thickness than the 0.2 mm layer thickness as printed road is less compressed and thus larger variance in the feature heights across the surface of the printed objects can be expected. As the layer thickness is increased to 0.3 mm, significant stringing of material across the surface, especially near the edge, is observed. There is a transition from unfilled regions to excess material that is pulled on the surface as the layer thickness is increased. This change may be associated with shear rate dependent rheological properties of the ABS [29]. The profiles for all of the specimens are shown in Figures S10, S11, and S12. Given the complexity

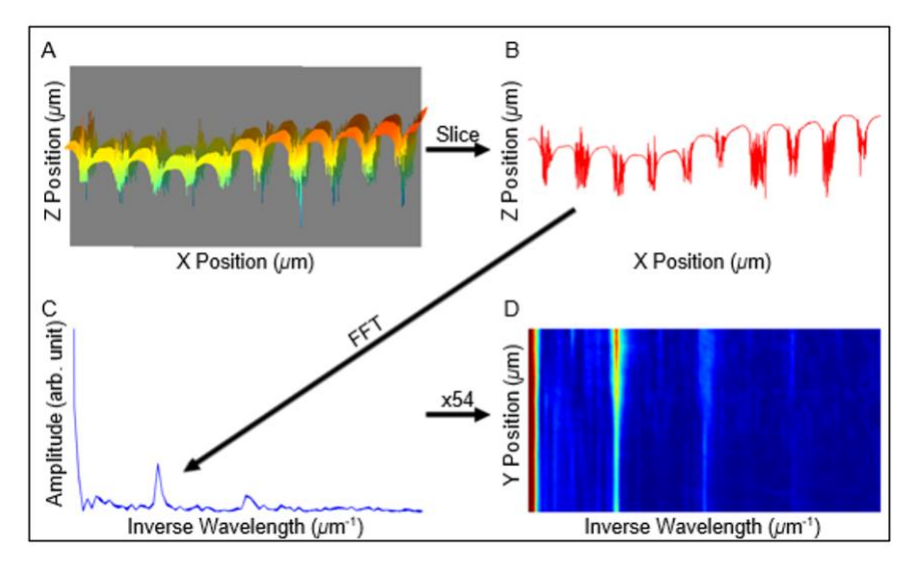
in the topology, it is difficult to assess what differences in the surface features may correspond with degraded mechanical performance of the part.



**Figure** Error! No text of specified style in document.. Representative surface morphology from optical profilometry within the gauge region prior to deformation as shown in Figure 1 using 90° raster angle printed with layer thicknesses of (A) 0.2 mm; (B) 0.25 mm; (C) and 0.3 mm. The sample number noted corresponds to the same specimen used for the tensile measurement in Figure 2.

The periodicity associated with the print path provides an opportunity to quantify the surface morphology in a reciprocal space. To better understand the differences in the surface structures, the profilometry profiles are examined in Fourier space. The selection of Fourier transforms for image analysis in this case is driven by the previous successes with Fourier transforms in other image-driven applications, such as reducing computational requirements for image tracking [54], deblurring of images [55], and interpolation in medical imaging [56]. Figure 5 illustrates the general process used in this work to convert the profilometry data to a Fourier space map; a 3D profile for the gauge region is obtained with an optical profilometer, the image is sliced for examination of correlations perpendicular to the printed road direction, and the Fourier transforms of the 1D profiles are used to create spatial maps of the printed topology in Fourier

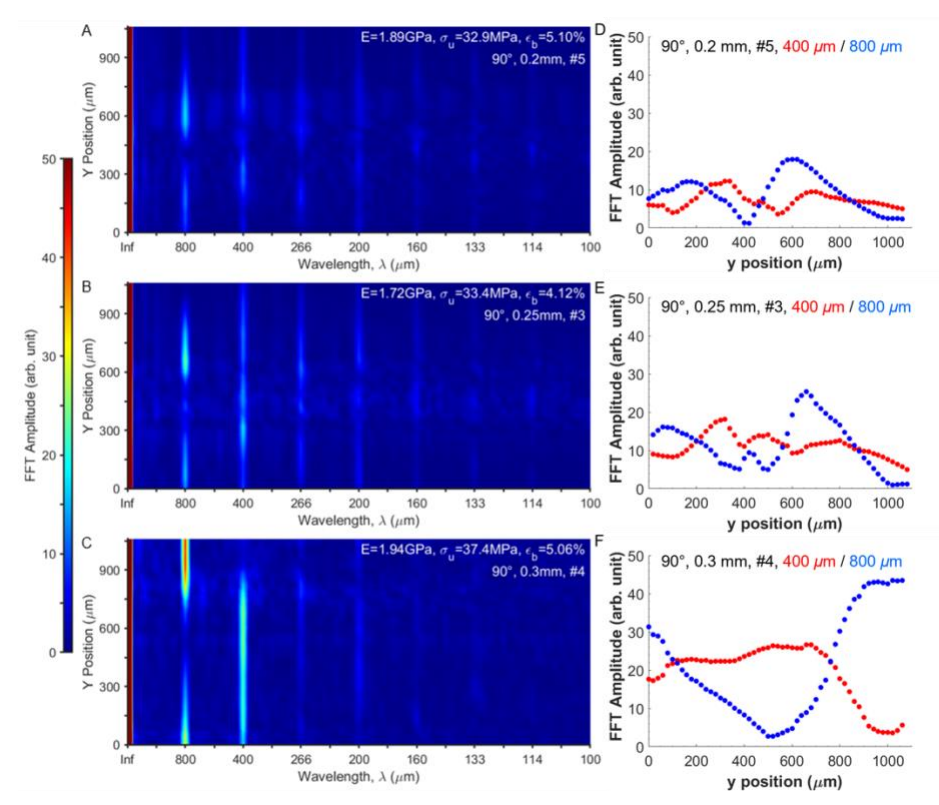
space. The discrete Fourier transform (DFT) of each line profile was converted into a single-sided amplitude spectrum (SSAS) describing the amplitude of each wave present in the surface with respect to frequency and combined to form a 3D representation of how the SSAS changes along the y-dimension.



**Figure 5.** Process of converting a 3D surface morphology measurement (SMM) into a set of single-sided amplitude spectra (SSASs). (A) A 3D SMM is sliced with an xz-plane every 20  $\mu$ m in the y-dimension; (B) producing line profiles which are then converted using a fast Fourier transform; (C) into an SSAS describing the waves contained within the individual line profile; and (D) combining SSASs to map the surface topology with respect to the y-dimension.

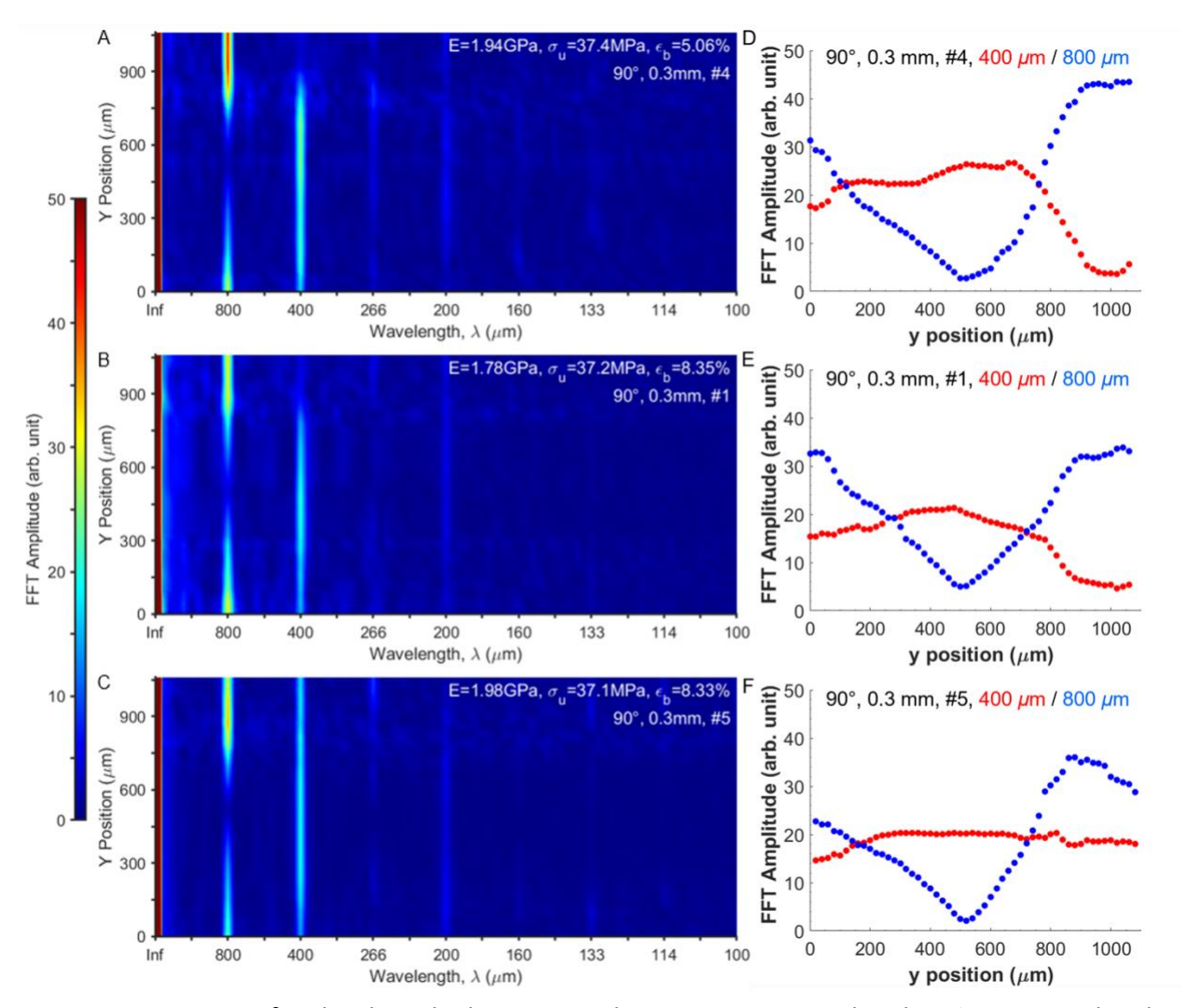
Figure 6 illustrates the SSAS maps for the real space profiles from Figure 4. The Fourier space representation of these thickness profiles are similar qualitatively with lines corresponding to length scale of correlations across and between printed roads. The data are presented in terms of an effective wavelength ( $\lambda$ ) that corresponds to the Fourier spacing for ease of interpretation. The road width was 400  $\mu$ m, which agrees well with one of the more intense lines in the SSAS maps for the 3 specimens. The other generally intense line is at 800  $\mu$ m, which is associated with two adjacent roads. The higher strength parts tend to have higher amplitudes for these two lines in the SSAS space. There are additional periodic lines in the maps that correspond to the integer multiples of the Fourier spacing corresponding to the road width, similar to the structures obtained from scattering or diffraction of lamellae nanostructures [57]. With 0.2 mm layer thickness, the correlation of two road width is high at around 250 and 600  $\mu$ m (Y position) across

the printed road; the structure is not as well defined near the edges of the specimen (low and high Y position) as might be expected with the acceleration and deceleration, but also in the middle of the specimen as the intensity of the SSAS decreases for both the 800 and 400  $\mu m$ wavelengths. These changes in correlations across the width of the specimen may be easier to visualize as a simple plot at these two wavelengths of interest as shown in Figure 6D. The loss of correlation in the middle of the specimen may be associated with the holes in the specimens. For the increase in layer thickness to 0.25 mm, the same qualitative SSAS map is found, but the intensity is increased for the 800 and 400 µm wavelengths as shown in Figure 6E, suggesting a more uniform structure with the increased layer thickness with less uniform road width near the edges of the specimen, although the correlations may be enhanced by the larger layer thickness that provides potential for higher contrast in thickness between roads. For the 0.3 mm layer thickness, there is a significant change in the SSAS map; the intensity of the correlation associated with the single road line width is much greater and there is a stronger two road correlation (800 μm) near the edges of the specimen as shown in Figure 6F. This correlation of the two roads weakens towards the center of the specimen. In examining the mechanical properties, there is an increase in the ultimate tensile strength ( $\sigma_u$ ) as the intensity of the lines associated with the 800 and 400 µm wavelengths increase in the SSAS.



**Figure 6.** Single-sided amplitude spectra of the specimens whose real space surface morphology is shown in Figure 4 with layer thicknesses of (A) 0.2 mm, (B) 0.25 mm, and (C) 0.3 mm. The corresponding amplitude profiles for the maxima at 400  $\mu$ m and 800  $\mu$ m as shown as a function of distance across the width of the specimen in the gauge region (Y position) for layer thickness of (D) 0.2 mm, (E) 0.25 mm, and (F) 0.3 mm.

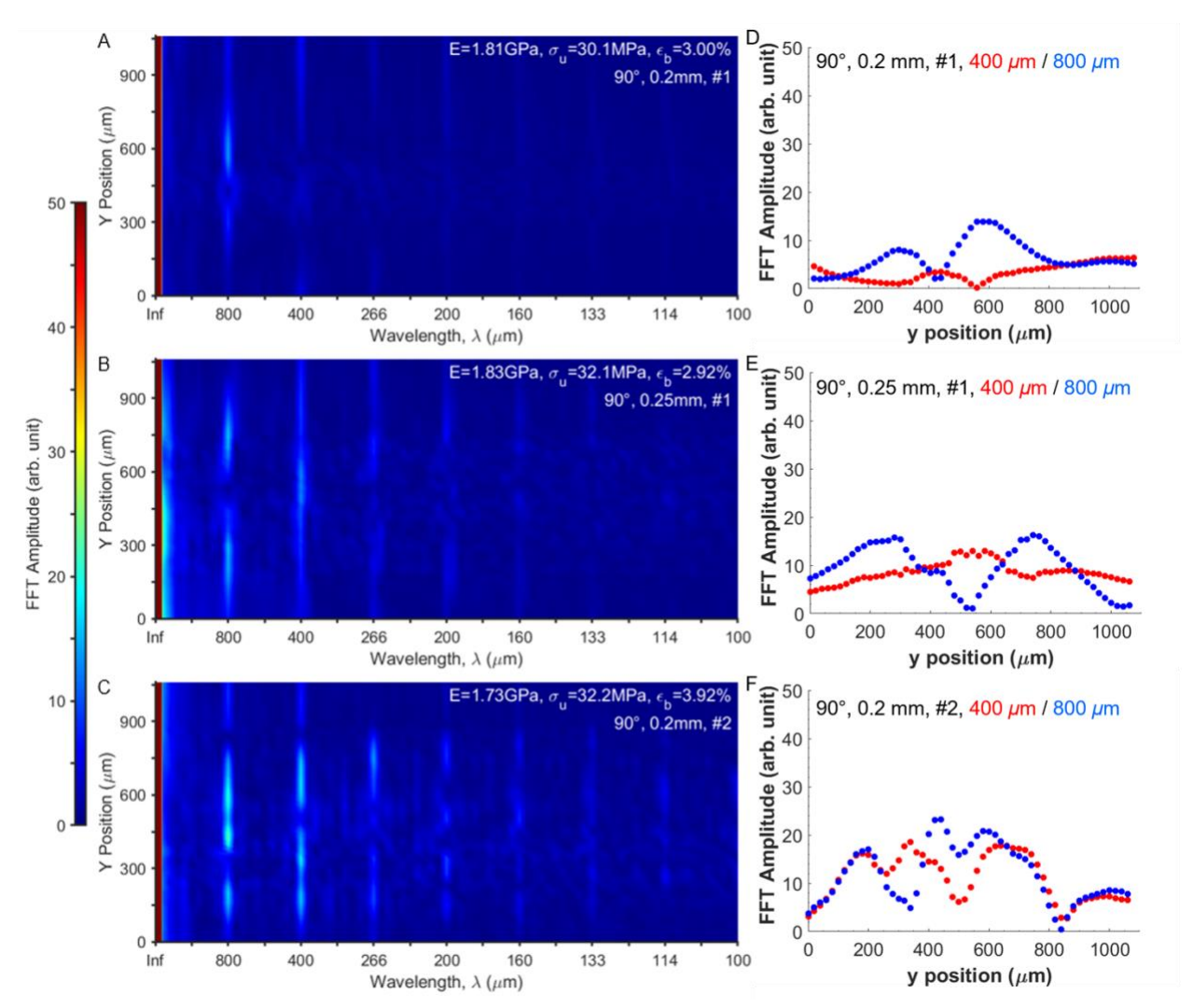
To better understand if there is a correlation between the surface structure and mechanical strength and these differences are not simply associated with the differences in the print conditions, the SSAS maps for the 3 strongest specimens are shown in Figure 7. Interestingly, the intensity for the road width (400  $\mu$ m) is high through the middle of specimen in every case as shown in Figure 7D-F. Moreover, the strong correlation in two road widths near to the edges is present in all three specimens. The similarity in these SSAS maps suggests that the SSAS correspond with the mechanical performance, so high tensile strength specimens could be identified nondestructively by optical profilometry. However, all these specimens are printed with the 0.3 mm layer thickness, so these characteristics could simply be associated with the print conditions.



**Figure 7.** SSAS maps for the three highest strength specimens printed with 90° raster angle. The corresponding amplitude profiles for the maxima at 400  $\mu$ m and 800  $\mu$ m as shown as a function of distance across the width of the specimen in the gauge region (Y position) for the three specimens.

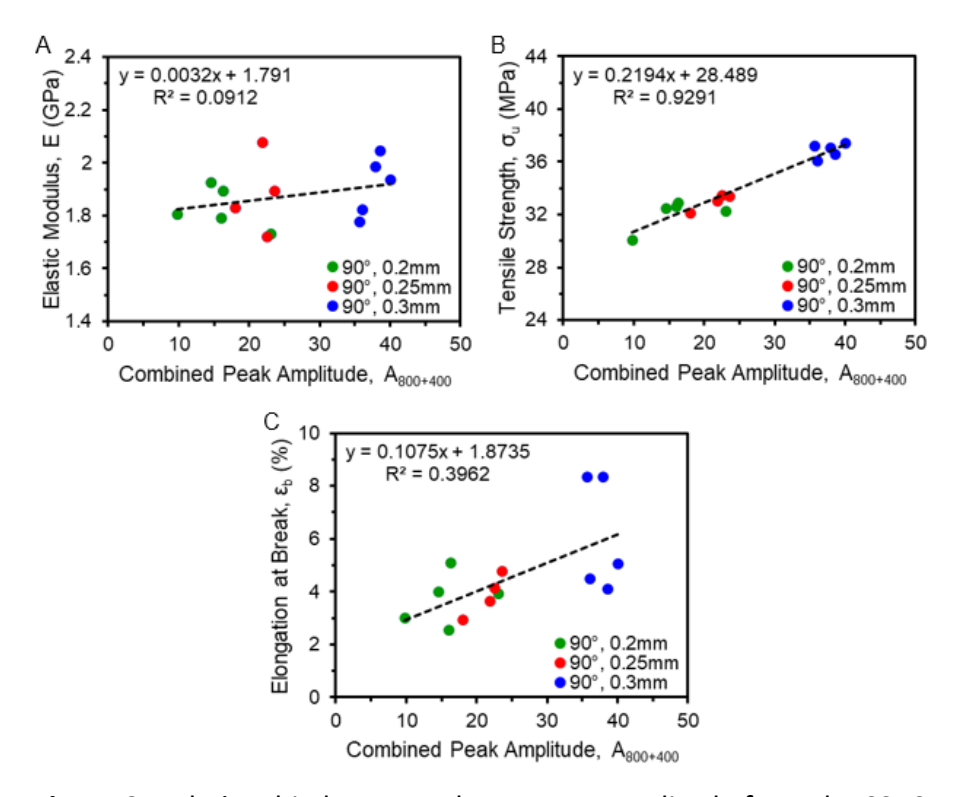
For quality control, identification of poor performance specimens would be valuable to decrease the lower variation in properties that lead to overdesign of parts to account for the statistical spread in performance. Figure 8 illustrates the SSAS for the 3 weakest specimens (lowest  $\sigma_u$ ) from the print trials. The intensity of the lines associated with the 800 and 400  $\mu$ m wavelengths are weak and nearly discontinuous across the specimen in the case of the 400  $\mu$ m wavelength. This loss in the correlations in the middle of the specimen is easier to see in the line cuts shown in

Figure 8D. For the weakest specimens, both 0.2 and 0.25 mm layer thicknesses are represented with the 0.25 mm specimen in Figure 8 exhibiting lower intensity of the two lines (400  $\mu$ m and 800  $\mu$ m wavelengths) than one of the 0.2 mm specimens. This suggests that the layer thickness is not the only factor that determines the intensity profiles in the SSAS maps. The SSAS maps for all of the specimens printed are shown in Figures S17-S19 for completeness.



**Figure 8.** SSAS maps for the 3 lowest strength specimens printed with 90° raster angle. The corresponding amplitude profiles for the maxima at 400  $\mu$ m and 800  $\mu$ m as shown as a function of distance across the width of the specimen in the gauge region (Y position) for the three specimens.

There appears to be a correlation between the intensity of the lines associated with the 800 and 400 µm wavelengths in the SSAS maps and the ultimate tensile strength of the printed specimens from these figures qualitatively. To examine this relationship more quantitatively, the average sum of the amplitudes across the specimens at 800 and 400 µm wavelength was calculated for each specimen. Figure 9 illustrates the relationship between the amplitude of these wavelengths in the SSAS and mechanical properties determined from tensile tests. There is no trend with respect to the elastic modulus as shown in Figure 9A; the values for the modulus are scattered as the small deformation that is responsible for the elastic response is not particularly sensitive to the larger scale features determined from optical profilometry. However, the ultimate tensile strength appears to be linearly correlated with this average amplitude (Figure 9B). This correlation is consistent with the qualitative results from visual examination of the SSAS. All ABS specimens yield after the ultimate tensile stress as shown in Figure S2. Thus, the ultimate tensile strength is a measure of the properties associated with yielding of the polymer, rather than failure, which would be more stochastic. The SSAS contains only surface topology information about the printed sample prior to deformation and it is highly unlikely that the correlations with UTS for individual specimens with the SSAS based primarily on defects that originate at the surface layer, rather the surface topology likely contains information about details in the printing of previous layers as well to provide the correlation with mechanical properties. Unlike the yield point, the strain at break generally depends on individual defects that nucleate and allow crack growth. The averaging by the FFT averages out these details and thus unsurprisingly, the strain at break is not correlated with the combined peak amplitude. A variety of other features in the SSAS maps were examined to understand if there was information in the profilometry data that can better describe the expected mechanical properties as described in the Supplementary Materials. None were able to provide a simple correlation to E or  $\varepsilon_b$  as information related to these properties may not translate as well through the layers of the print. Nonetheless, these data illustrate that post-print profilometric imaging offers potential for non-destructive characterization to identify parts with low tensile strength, which could be beneficial for improving the reliability of additively manufactured plastic parts through the use of profilometry as part of the quality control measures.



**Figure 9.** Relationship between the average amplitude from the SSAS maps for the 800 and 400 μm lines and (A) elastic modulus, (B) tensile strength and (C) elongation at break. There is a clear correlation of the SSAS features and the tensile strength.

As the correlations between the surface morphology and the mechanical properties were determined from the Fourier transform, the sensitivity is to variations in the periodicity of the structure. Increasing the size of the specimen examined will decrease the fraction of the specimen that is near to the edges of the sample. This effect can be observed through comparison of the FFT for the gauge (Figures S17A, S18A and S19A) and grips (Figure S16) section for specimen #1 at the 3 different layer thicknesses using 90° raster angle; These is a significant difference in the SSAS for the same specimens when examined in different areas. This sensitivity of the FFT is associated with reduced correlations near the edges due to the nature of the print path. As the same specimen exhibit distinct SSAS depending on the location examined, changes in the size of the specimen will alter the potential size of the surface that can be probed and the details of the correlation between the FFT and mechanical properties. Additionally, large changes in the total

number of layers would impact the surface topology to limit the ability to compare specimens at that significantly different. Thus, this methodology would be useful for quality control through examination of an invariant region of a 3D printed product that is only modestly customized. However, not all changes in the print path for the object lead to a loss in the correlations between the SSAS and mechanical property; the data presented uses different layer thickness to generate the correlations and the number of layers in the objects was changed to obtain a common thickness. Additional work is necessary to precisely determine what process parameters can be altered without a loss in the correlations between UTS and the SSAS.

As the Fourier transforms were selected for the ease in implementation, alternative image analyses may be more effective and generalizable for correlations between the surface topology and mechanical performance of individual printed objects. This work provides the proof of concept that the mechanical properties can be non-destructively elucidated from surface topology after appropriate calibration. With the large parameter space and desired for customization with AM, more advanced image analyses, such as machine learning, may enable more generalized approaches for quality control assessment.

## 4. CONCLUSIONS

The potential of using surface topology to predict mechanical performance of ABS produced by MEAM was explored. With a Type V tensile bar, the mechanical properties were only marginally dependent on raster angle and layer thickness. The surface morphology of the printed parts with 90° raster angle, however, was significantly impacted by these selections, but the differences can be difficult to clearly understand. Through application of a 1D Fourier transform, Fourier space maps of the surface topology of the printed parts prior to deformation were generated that illustrated clear differences in the amplitude of the spatial correlations associated with the wavelength for the printed road width and two roads. By examining each individual printed specimen, the variance in tensile strength can be understood from these differences. There is a linear correlation between the tensile strength of a given specimen and the amplitude in Fourier space for the road and two road widths. These results suggest that information is transferred

between layers in MEAM such that the tensile strength of specimens printed at the same conditions can be determined from the surface topology. However, this correlation requires the generation of a calibration curve between the structure of the printed object and the tensile strength. The Fourier analysis did not lead to a clear correlation with elastic moduli or the elongation at break for the printed specimens; this may be attributed to (1) the difference in the length scales of the deformation associated with the elastic modulus and topology imaging and (2) averaging of the imaging by the FFT and the point defect loci of failure common to control elongation at break. Nonetheless, these results illustrate the potential of optical profilometry to assess sample-to-sample variability in mechanical properties through the subtle differences in topology that indicate information transfer between printed layers, which could be useful for quality control measures during additive manufacturing.

#### **DECLARATIONS**

Conflict of interest statement: On behalf of all authors, the corresponding author states that there is no conflict of interest.

Supplementary Materials: Additional experimental details and data are available online as supplementary materials.

#### 5. REFERENCES

- (1) Garcia-Dominguez, A.; Claver, J.; Sebastian, M. A. (2020) Optimization Methodology for Additive Manufacturing of Customized Parts by Fused Deposition Modeling (FDM). Application to a Shoe Heel. Polymers 12:2119. https://doi.org/10.3390/polym12092119.
- (2) Tofail, S. A. M.; Koumoulos, E. P.; Bandyopadhyay, A.; Bose, S.; O'Donoghue, L.; Charitidis, C. (2018) Additive manufacturing: scientific and technological challenges, market uptake and opportunities. Materials Today 21:22-37. https://doi.org/10.1016/j.mattod.2017.07.001.
- (3) Zeltmann, S. E.; Gupta, N.; Tsoutsos, N. G.; Maniatakos, M.; Rajendran, J.; Karri, R.(2016) Manufacturing and Security Challenges in 3D Printing. JOM 68:1872-1881. https://doi.org/10.1007/s11837-016-1937-7.
- (4) Kumar, S.; Czekanski, A. (2018) Roadmap to sustainable plastic additive manufacturing. Materials Today Communications 15:109-113. https://doi.org/10.1016/j.mtcomm.2018.02.006.
- (5) Ma, J. F.; Harstvedt, J. D.; Dunaway, D.; Bian, L. K.; Jaradat, R. (2018) An exploratory investigation of Additively Manufactured Product life cycle sustainability assessment. Journal of Cleaner Production 192:55-70. https://doi.org/10.1016/j.jclepro.2018.04.249.

- (6) Pascu, N. E.; Arion, A. F.; Dobrescu, T.; Carutasu, N. L. (2015) Fused Deposition Modeling Design Rules for Plastics. Materiale Plastice 52:141-143.
- (7) Cano-Vicent, A.; Tambuwala, M. M.; Hassan, S. S.; Barh, D.; Aljabali, A. A. A.; Birkett, M.; Arjunan, A.; Serrano-Aroca, A. (2021) Fused deposition modelling: Current status, methodology, applications and future prospects. Additive Manufacturing 47:102378. https://doi.org/10.1016/j.addma.2021.102378.
- (8) Turner, B. N.; Gold, S. A. (2015) A review of melt extrusion additive manufacturing processes: II. Materials, dimensional accuracy, and surface roughness. Rapid Prototyping Journal 21:250-261. https://doi.org/10.1108/rpj-02-2013-0017.
- (9) Durgun, I.; Ertan, R. (2014) Experimental investigation of FDM process for improvement of mechanical properties and production cost. Rapid Prototyping Journal 20:228-235, Article. https://doi.org/10.1108/rpj-10-2012-0091.
- (10) Chohan, J. S.; Mittal, N.; Kumar, R.; Singh, S.; Sharma, S.; Singh, J.; Rao, K. V.; Mia, M.; Pimenov, D. Y.; Dwivedi, S. P. (2020) Mechanical Strength Enhancement of 3D Printed Acrylonitrile Butadiene Styrene Polymer Components Using Neural Network Optimization Algorithm. Polymers 12:2250. https://doi.org/10.3390/polym12102250.
- (11) Mohamed, O. A.; Masood, S. H.; Bhowmik, J. L. (2015) Optimization of fused deposition modeling process parameters: a review of current research and future prospects. Advances in Manufacturing 3:42-53. https://doi.org/10.1007/s40436-014-0097-7.
- (12) Spoerk, M.; Arbeiter, F.; Cajner, H.; Sapkota, J.; Holzer, C. (2017) Parametric optimization of intra- and inter-layer strengths in parts produced by extrusion-based additive manufacturing of poly(lactic acid). Journal of Applied Polymer Science 134:45401. https://doi.org/10.1002/app.45401.
- (13) Street, D. P.; Ledford, W. K.; Allison, A. A.; Patterson, S.; Pickel, D. L.; Lokitz, B. S.; Messman, J. M.; Kilbey, S. M. (2019) Self-Complementary Multiple Hydrogen-Bonding Additives Enhance Thermomechanical Properties of 3D-Printed PMMA Structures. Macromolecules 52:5574-5582. https://doi.org/10.1021/acs.macromol.9b00546.
- (14) Perryman, S. C.; Dadmun, M. D. (2021) Incorporating crosslinks in fused filament fabrication: Molecular insight into post deposition reactions. Additive Manufacturing 38:101746. https://doi.org/10.1016/j.addma.2020.101746.
- (15) Valino, A. D.; Dizon, J. R. C.; Espera, A. H.; Chen, Q. Y.; Messman, J.; Advincula, R. C. (2019) Advances in 3D printing of thermoplastic polymer composites and nanocomposites. Progress in Polymer Science 98: 101162.. https://doi.org/10.1016/j.progpolymsci.2019.101162.
- (16) D'Amico, T.; Peterson, A. M. (2020) Bead parameterization of desktop and room-scale material extrusion additive manufacturing: How print speed and thermal properties affect heat transfer. Additive Manufacturing 34:101239. https://doi.org/10.1016/j.addma.2020.101239.
- (17) Wang, P.; Zou, B.; Ding, S. L. (2019) Modeling of surface roughness based on heat transfer considering diffusion among deposition filaments for FDM 3D printing heat-resistant resin.

- Applied Thermal Engineering 161:114064. https://doi.org/10.1016/j.applthermaleng.2019.114064.
- (18) Van de Voorde, B.; Katalagarianakis, A.; Huysman, S.; Toncheva, A.; Raquez, J. M.; Duretek, I.; Holzer, C.; Cardon, L.; Bernaerts, K. V.; Van Hemelrijck, D.; et al. (2022) Effect of extrusion and fused filament fabrication processing parameters of recycled poly(ethylene terephthalate) on the crystallinity and mechanical properties. Additive Manufacturing 50:102518. https://doi.org/10.1016/j.addma.2021.102518.
- (19) El Magri, A.; El Mabrouk, K.; Vaudreuil, S.; Chibane, H.; Touhami, M. E. (2020) Optimization of printing parameters for improvement of mechanical and thermal performances of 3D printed poly(ether ether ketone) parts. Journal of Applied Polymer Science 137:49087. https://doi.org/10.1002/app.49087.
- (20) Farzadi, A.; Solati-Hashjin, M.; Asadi-Eydivand, M.; Abu Osman, N. A. Effect of Layer Thickness and Printing Orientation on Mechanical Properties and Dimensional Accuracy of 3D Printed Porous Samples for Bone Tissue Engineering. Plos One **2014**, 9 (9), e108252. HTTPS://DOI.ORG/10.1371/journal.pone.0108252.
- (21) Laureto, J. J.; Pearce, J. M. (2018) Anisotropic mechanical property variance between ASTM D638-14 type i and type iv fused filament fabricated specimens. Polymer Testing 68:294-301. https://doi.org/10.1016/j.polymertesting.2018.04.029.
- (22) Ponsar, H.; Wiedey, R.; Quodbach, J. (2020) Hot-Melt Extrusion Process Fluctuations and Their Impact on Critical Quality Attributes of Filaments and 3D-Printed Dosage Forms. Pharmaceutics 12:511. https://doi.org/10.3390/pharmaceutics12060511.
- (23) Koker, B.; Ruckdashel, R.; Abajorga, H.; Curcuru, N.; Pugatch, M.; Dunn, R.; Kazmer, D. O.; Wetzel, E. D.; Park, J. H. (2022) Enhanced interlayer strength and thermal stability via dual material filament for material extrusion additive manufacturing. Additive Manufacturing 55:102807. https://doi.org/10.1016/j.addma.2022.102807.
- (24) Coogan, T. J.; Kazmer, D. O. (2019) Modeling of interlayer contact and contact pressure during fused filament fabrication. Journal of Rheology 63:655-672. https://doi.org/10.1122/1.5093033.
- (25) Anderegg, D. A.; Bryant, H. A.; Ruffin, D. C.; Skrip, S. M.; Fallon, J. J.; Gilmer, E. L.; Bortner, M. J. (2019) In-situ monitoring of polymer flow temperature and pressure in extrusion based additive manufacturing. Additive Manufacturing 26:76-83. https://doi.org/10.1016/j.addma.2019.01.002.
- (26) Agassant, J. F.; Pigeonneau, F.; Sardo, L.; Vincent, M. (2019) Flow analysis of the polymer spreading during extrusion additive manufacturing. Additive Manufacturing 29: 100794. https://doi.org/10.1016/j.addma.2019.100794.
- (27) McIlroy, C.; Olmsted, P. D. (2017) Deformation of an amorphous polymer during the fused-filament-fabrication method for additive manufacturing. Journal of Rheology 61:379-397. https://doi.org/10.1122/1.4976839.

- (28) Monzon, M. D.; Gibson, I.; Benitez, A. N.; Lorenzo, L.; Hernandez, P. M.; Marrero, M. D. (2013) Process and material behavior modeling for a new design of micro-additive fused deposition. International Journal of Advanced Manufacturing Technology 67:2717-2726. https://doi.org/10.1007/s00170-012-4686-y.
- (29) Das, A.; Gilmer, E. L.; Biria, S.; Bortner, M. J. (2021) Importance of Polymer Rheology on Materials Extrusion Additive Manufacturing: Correlating Process Physics to Print Properties. ACS Applied Polymer Materials 3:1218-1249. https://doi.org/10.1021/acsapm.0c01228.
- (30) Comminal, R.; Serdeczny, M. P.; Pedersen, D. B.; Spangenberg, J. (2019) Motion planning and numerical simulation of material deposition at corners in extrusion additive manufacturing. Additive Manufacturing 29:100753. https://doi.org/10.1016/j.addma.2019.06.005.
- (31) Costanzo, A.; Spotorno, R.; Candal, M. V.; Fernandez, M. M.; Mueller, A. J.; Graham, R. S.; Cavallo, D.; McIlroy, C. (2020) Residual alignment and its effect on weld strength in material-extrusion 3D-printing of polylactic acid. Additive Manufacturing 36:101415. https://doi.org/10.1016/j.addma.2020.101415.
- (32) Gilmer, E. L.; Miller, D.; Chatham, C. A.; Zawaski, C.; Fallon, J. J.; Pekkanen, A.; Long, T. E.; Williams, C. B.; Bortner, M. J. (2018) Model analysis of feedstock behavior in fused filament fabrication: Enabling rapid materials screening. Polymer 152:51-61. https://doi.org/10.1016/j.polymer.2017.11.068.
- (33) Samy, A. A.; Golbang, A.; Harkin-Jones, E.; Archer, E.; McIlhagger, A. (2021) Prediction of part distortion in Fused Deposition Modelling (FDM) of semi-crystalline polymers via COMSOL: Effect of printing conditions. CIRP Journal of Manufacturing Science and Technology 33:443-453. https://doi.org/10.1016/j.cirpj.2021.04.012.
- (34) Romano, S.; Brandao, A.; Gumpinger, J.; Gschweitl, M.; Beretta, S. (2017) Qualification of AM parts: Extreme value statistics applied to tomographic measurements. Materials & Design 131:32-48. https://doi.org/10.1016/j.matdes.2017.05.091.
- (35) Cummings, I.; Hillstrom, E.; Newton, R.; Flynn, E.; Wachtor, A. In-Process Ultrasonic Inspection of Additive Manufactured Parts. In 34th IMAC Conference and Exposition on Structural Dynamics, Orlando, FL, Jan 25-28, 2016; pp 235-247. https://doi.org/10.1007/978-3-319-30249-2 20.
- (36) AbouelNour, Y.; Gupta, N. (2022) In-situ monitoring of sub-surface and internal defects in additive manufacturing: A review. Materials & Design 222: 111063. https://doi.org/10.1016/j.matdes.2022.111063.
- (37) Chen, Y.; Peng, X.; Kong, L. B.; Dong, G. X.; Remani, A.; Leach, R. (2021) Defect inspection technologies for additive manufacturing. International Journal of Extreme Manufacturing 3:022002. https://doi.org/10.1088/2631-7990/abe0d0.
- (38) Cerniglia, D.; Scafidi, M.; Pantano, A.; Rudlin, J. (2015) Inspection of additive-manufactured layered components. Ultrasonics 62: 292-298. https://doi.org/10.1016/j.ultras.2015.06.001.

- (39) Metel, A. S.; Tarasova, T.; Skorobogatov, A.; Podrabinnik, P.; Volosova, M.; Grigoriev, S. N. (2023) Quality Diagnostics of Parts Produced by Combined Additive Manufacturing Technology. Metals 13:19. https://doi.org/10.3390/met13010019.
- (40) Liu, R. S.; Vogt, B. D.; Yang, H. (2021) Gaussian Process Monitoring of Layerwise-Dependent Imaging Data. IEEE Robotics and Automation Letters 6:8029-8036. https://doi.org/10.1109/lra.2021.3102625.
- (41) Sun, X. C.; Mazur, M.; Cheng, C. T. (2023) A review of void reduction strategies in material extrusion-based additive manufacturing. Additive Manufacturing 67:103463. https://doi.org/10.1016/j.addma.2023.103463.
- (42) Liu, C. X.; Yang, C. L.; Liu, J.; Tang, Y. J.; Lin, Z. J.; Li, L.; Liang, H.; Lu, W. J.; Wang, L. Q. (2023) Error assessment and correction for extrusion-based bioprinting using computer vision method. International Journal of Bioprinting 9:299-308. https://doi.org/10.18063/ijb.v9i1.644.
- (43) Wichniarek, R.; Hamrol, A.; Kuczko, W.; Gorski, F.; Rogalewicz, M. (2021) ABS filament moisture compensation possibilities in the FDM process, CIRP Journal of Manufacturing Science and Technology 35:550-559. <a href="https://doi.org/10.1016/j.cirpj.2021.08.011">https://doi.org/10.1016/j.cirpj.2021.08.011</a>
- (44) Ai, J. R.; Vogt, B. D. (2022) Size and print path effects on mechanical properties of material extrusion 3D printed plastics. Progress in Additive Manufacturing **7**:1009-1021. https://doi.org/10.1007/s40964-022-00275-w.
- (45) Zhang, Y.K.; Shen, S.N.; Li, H.; Hu, Y.W. (2022) Review of in situ and real-time monitoring of metal additive manufacturing based on image processing, International Journal of Advanced Manufacturing Technology 123:1-20. https://doi.org/10.1007/s00170-022-10178-3
- (46) Mahato, V.; Obeidi, M.A.; Brabazon, D.; Cunningham, P. (2022) Detecting voids in 3D printing using melt pool time series data, Journal of Intelligent Manufacturing 33:845-852. https://doi.org/10.1007/s10845-020-01694-8
- (47) Gasior, M.; Gonzalez, J. L. Improving FFT frequency measurement resolution by parabolic and Gaussian spectrum interpolation. In 11th Beam Instrumentation Workshop, Spallat Neutron Source, Knoxville, TN, May 03-06, 2004; pp 276-285.
- (48) Franchetti, F.; Karner, H.; Kral, S.; Ueberhuber, C. W. Architecture independent short vector FFTs. In IEEE International Conference on Acoustics, Speech, and Signal Processing, Salt Lake City, UT, May 07-11, 2001; pp 1109-1112.
- (49) Kakanuru, P.; Pochiraju, K. (2020) Moisture Ingress and Degradation of Additively Manufactured PLA, ABS and PLA/SiC Composite Parts, Additive Manufacturing 36:101529. <a href="https://doi.org/10.1016/j.addma.2020.101529">https://doi.org/10.1016/j.addma.2020.101529</a>
- (50) Striemann, P.; Huelsbusch, D.; Niedermeier, M.; Walther, F. (2021) Application-oriented assessment of the interlayer tensile strength of additively manufactured polymers. Additive Manufacturing 46: 102095. https://doi.org/10.1016/j.addma.2021.102095.

- (51) Zaldivar, R. J.; Witkin, D. B.; McLouth, T.; Patel, D. N.; Schmitt, K.; Nokes, J. P. (2017) Influence of processing and orientation print effects on the mechanical and thermal behavior of 3D-Printed ULTEM (R) 9085 Material. Additive Manufacturing 13:71-80. https://doi.org/10.1016/j.addma.2016.11.007.
- (52) Fleming, T. G.; Nestor, S. G. L.; Allen, T. R.; Boukhaled, M. A.; Smith, N. J.; Fraser, J. M. (2020) Tracking and controlling the morphology evolution of 3D powder-bed fusion in situ using inline coherent imaging. Additive Manufacturing 32:1009178. https://doi.org/10.1016/j.addma.2019.100978.
- (53) Zhou, Y.; Ghim, Y. S.; Fard, A.; Davies, A. (2013) Application of the random ball test for calibrating slope-dependent errors in profilometry measurements. Applied Optics 52: 5925-5931. https://doi.org/10.1364/ao.52.005925.
- (54) Henriques, J.F.; Caseiro, R.; Martins, P.; Batista, J. (2015) High-Speed Tracking with Kernelized Correlation Filters, IEEE Transactions on Pattern Analysis and Machine Intelligence 37:583-596. https://doi.org/ 10.1109/TPAMI.2014.2345390
- (55) Wang, Y.L.; Yang, J.F.; Yin, W.T.; Zhang, Y. (2008) A New Alternating Minimization Algorithm for Total Variation Image Reconstruction, SIAM Journal on Imaging Sciences 1:248-272. https://doi.org/10.1137/08072426
- (56) Lehmann, T.M.; Gonner, C.; Spitzer, K. (1999) Survey: Interpolation methods in medical image processing, IEEE Transactions on Medical Imaging 18:1049-1075. https://doi.org/10.1109/42.816070
- (57) Zhu, L.; Cheng, S. Z. D.; Calhoun, B. H.; Ge, Q.; Quirk, R. P.; Thomas, E. L.; Hsiao, B. S.; Yeh, F. J.; Lotz, B. (2000) Crystallization temperature-dependent crystal orientations within nanoscale confined lamellae of a self-assembled crystalline-amorphous diblock copolymer. Journal of the American Chemical Society 122:5957-5967. https://doi.org/10.1021/ja000275e.